

# A New Model for the Extragalactic Radio Sky at Low Frequency Calibrated Using the LOFAR Two-metre Survey

Jinyang Lin,<sup>1</sup> Zhenghao Zhu,<sup>2\*</sup> Renyi Ma,<sup>1†</sup> Anna Bonaldi,<sup>3</sup> Huanyuan Shan<sup>2,4,5‡</sup>

<sup>1</sup>*Department of Astronomy and Institute of Theoretical Physics and Astrophysics, Xiamen University, Xiamen, Fujian 361005, China*

<sup>2</sup>*Shanghai Astronomical Observatory, Chinese Academy of Sciences, 80 Nandan Road, Shanghai 200030, China*

<sup>3</sup>*SKA Observatory, Jodrell Bank, Lower Whittington, Macclesfield, SK11 9DL, UK*

<sup>4</sup>*Key Laboratory of Radio Astronomy and Technology, Chinese Academy of Sciences, A20 Datun Road, Chaoyang District, Beijing, 100101, P. R. China*

<sup>5</sup>*University of Chinese Academy of Sciences, Beijing 100049, China*

Accepted XXX. Received YYY; in original form ZZZ

## ABSTRACT

Building the radio sky template are crucial for detecting the 21 cm emission line signal from the Epoch of Reionization (EoR), as well as for other cosmological research endeavors. Utilizing data from the LOFAR Two-meter Sky Survey (LoTSS) at 150 MHz, we recalibrated the luminosity function for various types of radio sources, including High Excitation Radio Galaxies (HERGs), Low Excitation Radio Galaxies (LERGs), Radio-Quiet Active Galactic Nuclei (RQ-AGNs), and Star-Forming Galaxies (SFGs). We subsequently updated the Tiered Radio Extragalactic Continuum Simulation (T-RECS) code to generate refined mock radio source catalogues. The simulated source counts from this work align more closely with observed data at redshifts greater than  $z > 4$ . Additionally, the differential source counts in total intensity within the flux density range of 0.1 – 1 mJy closely mirror actual observations. Due to our model incorporating a lower number of faint sources compared to T-RECS, it predicts a reduced power spectrum for point sources, suggesting a potential advantage in studies in low frequency band.

**Key words:** radio continuum: galaxies – galaxies: luminosity function, mass function – methods: numerical

## 1 INTRODUCTION

As well known, intensity maps of 21 cm emission line at redshift around  $z \sim 6$  and beyond provide us with an important and unique probe to investigate the physics at the Epoch of Reionization (EoR, Pritchard & Loeb 2012). However, the reionization signal encounters significant challenges from systematic contamination due to foreground radiation, i.e., the local emission from the Milky Way, the diffuse and compact extragalactic sources (Di Matteo et al. 2002; de Oliveira-Costa et al. 2008; Bowman et al. 2009; Jelić et al. 2008, 2010; Spinelli et al. 2018; Chapman & Jelić 2019).

The compact extragalactic point sources have been estimated to contribute approximately 27% of the total foreground radiation at 150 MHz (Shaver et al. 1999). Particularly in the context of small-scale regions within the power spectrum, extragalactic point sources emerge as the most important foreground element (Procopio et al. 2017; Murray et al. 2017; Yoshiura et al. 2018).

The point sources can be classified as Active Galactic Nuclei (AGNs) and Star Formation Galaxies (SFGs). For non-AGN sources, both the synchrotron radiation emitted by relativistic electrons associated with supernovae, as well as the free-free emission from HII regions, contribute to the radio emission (Helou et al. 1985; Condon 1992; Jarvis et al. 2010), while for AGNs, because of the release of huge gravitational energy as the gas falls towards the central black

holes, all the components of the accretion system are capable of producing radio emission. Based on the radio loudness, i.e., the ratio of the radio to optical luminosity, AGNs are divided into radio-loud (RL) and radio-quiet (RQ) types, which constitute approximately 10% and 90% of the AGN population, respectively (Kellermann et al. 1989; Sikora et al. 2007).

The radio luminosity of RL AGNs is dominated by the relativistic jets, in which high-energy electrons are accelerated and then emit synchrotron photons in the strong collimating magnetic fields (e.g. Blandford et al. 2019). Considering the geometry of the radio image, it can be further divided into FRI and FRII sub-populations (Fanaroff & Riley 1974). Considering the different optical and ultraviolet spectral features, which should be due to the different accretion modes that are efficient or non-efficient in radiation, RL AGNs are also divided into HERGs and LERGs (Heckman & Best 2014; Hardcastle & Croston 2020). In contrast, the origins of radio emission in RQ-AGNs remain unclear (Panessa et al. 2019), though different models have been postulated, including star formation activities like SFGs (Sopp & Alexander 1991), the diminutive jets (Ho & Ulvestad 2001), the corona (Laor & Behar 2008), and the disk winds (Wang 2008).

Radio sky simulation is a useful tool in quite a few aspects of astronomy. For example, it can be used to assess the completeness of radio surveys or to predict the population of radio sources that will be observed in given or future surveys; It was applied to test clustering theories of cosmology by generating random samples. Very important to us, in the research of reionization, it provides a way to predict the foreground noise of the 21 cm signal (e.g. Wilman et al. 2008, 2010; Bonaldi et al. 2019, 2023; Best et al. 2023).

\* zhenghao@shao.ac.cn

† ryma@xmu.edu.cn

‡ hyshan@shao.ac.cn

The Tiered Radio Extragalactic Continuum Simulation (T-RECS) (Bonaldi et al. 2019, 2023) is designed to simulate two primary populations of radio galaxies, i.e., AGNs and SFGs. It takes into account not only the luminosity functions for different redshift, but also the clustering properties (Baugh et al. 2019). However, since its luminosity function at 150 MHz is mainly obtained by extrapolating observations at higher frequencies, such as 1.4 GHz and 4.8 GHz, discrepancies between derived low-frequency simulations and actual low-frequency observations are induced.

In recent years, the deeper and more extensive low-frequency radio sky surveys (Hurley-Walker et al. 2017; Shimwell et al. 2017; Hurley-Walker et al. 2019; Shimwell et al. 2019; White et al. 2020; Franzen et al. 2021a; Sabater et al. 2021; Kondapally et al. 2021; Duncan et al. 2021; Best et al. 2023) have provided a wealth of data, significantly enhancing our capacity to refine simulations of the low-frequency radio sky. Among these surveys, the Low-Frequency Array Two-metre Sky Survey (LoTSS) Deep Fields is the most comprehensive deep radio survey ever conducted. In the recent survey by Best et al. (2023), the authors provided approximately 80,000 identified radio sources with matched information like stellar mass, star formation rate, etc.. The sources are therefore classified into four categories: HERGs, LERGs, RQ-AGNs, and SFGs. Compared to T-RECS, on the one hand, this catalogue offers more diverse sources such as RQ-AGNs, which are not modeled in T-RECS. On the other hand, the catalogue includes sources with higher redshift, which directly removes the discrepancies in source counts at high redshifts (Best et al. 2023).

The forthcoming observations by the Square Kilometre Array (SKA) represent a significant milestone in radio astronomy. The insights obtained through SKA's observations will challenge existing models. Currently, developing more precise simulations is crucial for forecasting SKA observations, addressing the challenges of detecting the EoR signal, and enhancing our understanding of extragalactic point sources.

In this paper, we present an updated classification of radio sources along with their corresponding evolutionary models. The paper is structured as follows: Section 2 outlines the data selection. Sections 3 introduces our models for AGN and SFG. In Section 4, we compare our model outputs with observed results and other simulations. Throughout our analysis, we employ cosmological parameters set to  $\Omega_m = 0.3$ ,  $\Omega_\Lambda = 0.7$  and  $H_0 = 70 \text{ km s}^{-1} \text{ Mpc}^{-1}$ .

## 2 DATA

As the radio emission is independent of dust, the deep radio survey offers a unique insight into the galaxies and AGN population. Based on the deep 150 MHz LoTSS survey in the three distinct sky region: ELAIS-N1, Boötes, and the Lockman Hole, which have been invested vast amounts of telescope time across the electromagnetic spectrum, Best et al. (2023) obtained a catalogue, which contains a total of 81,951 sources, with the lower flux limit of 0.003 mJy and the redshift range from 0 to 7. Here we adopted this catalogue to better model the galaxy evolution across cosmic time.

Based on detailed spectral energy distribution fitting, the sources were classified into four categories. Sources of low radio flux density are classified as SFGs or RQ-AGN depending on whether the spectra are AGN-like or not; while sources of high radio flux density are classified as LERGs and HERGs according to the luminosity.

Following Best et al. (2023), the classification of sources is performed by comparing four different spectral energy distribution (SED) codes: MAGPHYS (da Cunha et al. 2008), BAGPIPES (Car-

nall et al. 2018, 2019), CIGALE (Burgarella et al. 2005; Noll et al. 2009; Boquien et al. 2019), and AGNFITTER (Calistro Rivera et al. 2016), with the latter two including models that account for contributions from AGN. By evaluating the results from these four codes, they determine whether the sources are radiative mode AGNs and assign an appropriate consensus star formation rate and stellar mass to each source. Finally, based on whether they are radiative mode AGNs, and using Equation (2) from Best et al. (2023)—which concerns the relationship between the expected radio emission from the star formation rate and the actual radio emission—the sources are further subdivided into high-excitation galaxies, low-excitation galaxies, star-forming galaxies, and radio-quiet AGNs.

As the extragalactic radio sources primarily consist of AGN and SFGs, this catalogue is ideal for the simulation of foreground sources of the 21 cm signal. Taking into account the incompleteness of faint sources and integrating results from completeness simulations by Kondapally et al. (2022) and Cochrane et al. (2023), we refined our selection criteria for sources. We focused on those with redshifts between 0 and 6 and a flux density threshold of 0.11 mJy, which is the lowest flux density at which completeness can be reliably evaluated. This adjusted selection process identified 77,495 sources, resulting in the exclusion of approximately 3,000 sources.

## 3 MODEL DESCRIPTION

### 3.1 luminosity function

As the starting point for the radio sky simulation, the measured luminosity functions of different source populations, as well as their cosmic evolution, are the base of the simulations. In order to take into account the above with a more complete catalogue given by Best et al. (2023), we fit the luminosity functions as follows. For details not mentioned in this chapter (e.g., dark matter simulation for galaxy clustering effect and position angle), we followed what is used in T-RECS model (Bonaldi et al. 2023).

#### 3.1.1 Luminosity functions for LERGs and HERGs

We adopted a redshift-dependent comoving luminosity function of double power law as described by Massardi et al. (2010) to represent HERGs and LERGs in units of  $\text{Mpc}^{-3} (\text{d log } L)^{-1}$ . The function is written as

$$\Phi(L, z) = \frac{N}{(L/L_\star)^a + (L/L_\star)^b}, \quad (1)$$

where  $a$ ,  $b$ ,  $L_\star$  and  $N$  are the two power indices, the characteristic luminosity and number of sources, respectively. The characteristic quantities of  $L_\star$  and  $N$  evolve with redshift in the following way:

$$\log N(z) = n_0 + n_1 \chi + n_2 \chi^2, \quad (2)$$

$$L_\star(z) = L_\star(0) \text{ dex} \left[ k_{\text{evo}} z \left( 2z_{\text{top}} - z^{m_{\text{ev}}} z_{\text{top}}^{(1-m_{\text{ev}})/(1+m_{\text{ev}})} \right) \right], \quad (3)$$

$$\chi \equiv \log(1+z), \quad (4)$$

$$z_{\text{top}} = z_{\text{top},0} + \frac{\delta z_{\text{top}}}{1 + L_\star(0)/L}, \quad (5)$$

**Table 1.** Best-fit parameters of the evolutionary model for HERGs and LERGs. The luminosity  $L_*$  is in  $\text{erg s}^{-1} \text{Hz}^{-1}$ 

Parameter	LERG	HERG
$a$	$-1.875^{+0.148}_{-0.157}$	$-2.694^{+0.348}_{-0.366}$
$b$	$0.736^{+0.011}_{-0.010}$	$0.636^{+0.021}_{-0.019}$
$n_0$	$-3.341^{+0.022}_{-0.021}$	$-4.479^{+0.059}_{-0.058}$
$n_1$	$-1.565^{+0.166}_{-0.167}$	$-2.178^{+0.324}_{-0.341}$
$n_2$	$-2.239^{+0.264}_{-0.245}$	$-0.151^{+0.433}_{-0.423}$
$\log L_*(0)$	$29.137^{+0.029}_{-0.031}$	$29.469^{+0.064}_{-0.062}$
$k_{\text{evo}}$	$4.459^{+0.528}_{-0.472}$	$2.616^{+0.683}_{-0.653}$
$z_{\text{top},0}$	$0.037^{+0.037}_{-0.023}$	$0.393^{+0.046}_{-0.052}$
$\delta z_{\text{top}}$	$0.335^{+0.037}_{-0.039}$	$0.164^{+0.110}_{-0.088}$
$m_{\text{ev}}$	$0.284^{+0.011}_{-0.010}$	$0.370^{+0.041}_{-0.030}$

where  $n_0 \equiv \log N(0)$ ,  $N(0)$  and  $L_*(0)$  are the characteristic quantities at present or  $z = 0$ ,  $|m_{\text{ev}}| < 1$  is a free parameter,  $z_{\text{top},0}$  and  $\delta z_{\text{top}}$  are two parameters that very roughly describes the redshift when the luminosity functions reach the top.

Then by fitting the data obtained from the catalogue by Best et al. (2023), all the parameters in the modelling luminosity functions can be determined. Here we use the Monte Carlo Markov Chain method to fit the data, which gives the distribution of probabilities for the parameters. We use the *emcee* code to do sampling, which is available online at <http://dan.iel.fm/emcee> (Foreman-Mackey et al. 2013). Additionally, during the calculation of the luminosity function for the LoTSS-Deep survey, we take into account the completeness simulations from Kondapally et al. (2022) and Cochrane et al. (2023) for the LoTSS-Deep survey. The best-fitting results of the parameters are shown in Table 1, and the contours of the samplings are shown in Figure 1 and Figure 2.

### 3.1.2 Luminosity functions for RQ-AGNs and SFGs

RQ-AGNs exhibit clear signs of AGN activity across various non-radio wavelengths, including X-rays, mid-infrared, and optical spectra. However, they lack the prominent large-scale radio jets seen in Radio-Loud AGN (RL-AGN), resulting in significantly weaker radio emission (Kellermann et al. 2016; Padovani 2016). Despite extensive study, the nature of RQ-AGNs remains a subject of ongoing debate. One unresolved question of significance concerns the source of radio emissions in RQ-AGNs. Observational evidence suggests two potential contributors: a central core and star formation processes. Research by Padovani et al. (2015); Bonzini et al. (2015) suggests that RQ-AGNs exhibit characteristics such as infrared-radio flux ratios, evolving radio luminosity functions, host galaxy colors, optical morphology, and stellar mass similar to those of star-forming systems. This suggests that radio emissions in RQ-AGNs are primarily driven by star formation (Kimball et al. 2011; Condon et al. 2013; Kellermann et al. 2016)). Conversely, White et al. (2015, 2017) contended that RQ-AGNs exhibit higher radio luminosities compared to SFGs with similar stellar masses. Mancuso et al. (2017) suggested that the conflicting findings may arise partly from variations in luminosity and redshift ranges considered in the studies mentioned above.

Considering that the radio emissions of SFGs and RQ-AGNs may have common origins, and recent studies suggest that all types of quasars exhibit a combination of jet and star formation activity (Mac-

**Table 2.** Best-fit results of the parameters of the evolutionary model for RQ-AGNs and SFGs.

Parameter	RQ-AGN	SFG
$C_0$	$-7.190^{+0.236}_{-0.250}$	$-2.057^{+0.017}_{-0.018}$
$C_1$	$3.327^{+0.462}_{-0.459}$	$-4.602^{+0.279}_{-0.286}$
$C_2$	$-2.204^{+0.539}_{-0.614}$	$-6.142^{+1.107}_{-1.176}$
$l_{\star_0}$	$27.812^{+0.058}_{-0.056}$	$29.131^{+0.023}_{-0.024}$
$l_{\star_1}$	$9.039^{+0.149}_{-0.164}$	$4.375^{+0.104}_{-0.112}$
$l_{\star_2}$	$-5.686^{+0.207}_{-0.233}$	$-2.480^{+0.107}_{-0.104}$
$\alpha_0$	$5.087^{+0.189}_{-0.182}$	$0.262^{+0.049}_{-0.045}$
$\alpha_1$	$-4.813^{+0.448}_{-0.450}$	$9.711^{+0.471}_{-0.436}$
$\alpha_2$	$2.117^{+0.827}_{-0.721}$	$-2.871^{+0.350}_{-0.404}$
$\sigma$	$0.339^{+0.004}_{-0.004}$	$0.303^{+0.003}_{-0.003}$

farlane et al. 2021), we applied the same function to both RQ-AGNs and SFGs, with the differences attributing to the value of parameters. The luminosity function is taken from a model initially applied to fit the luminosity function of Infrared Astronomical Satellite (IRAS) galaxies (Saunders et al. 1990), which is written as

$$\Phi(L, z) = C \left( \frac{L}{L_{\star}} \right)^{\alpha} \exp \left\{ -\frac{1}{2} \left[ \frac{\log(1 + L/L_{\star})}{\sigma} \right]^2 \right\} \quad (6)$$

$$C(z) = C_0 + C_1 \chi + C_2 \chi^2 \quad (7)$$

$$\log L_{\star}(z) = l_{\star_0} + l_{\star_1} \chi + l_{\star_2} \chi^2 \quad (8)$$

$$\alpha(z) = \alpha_0 + \alpha_1 \chi + \alpha_2 \chi^2 \quad (9)$$

Similar to the fitting of LERGs and HERGs, the parameters for SFGs and RQ-AGNs are derived by fitting the data from LoTSS with MCMC method. The value of the parameters are shown in Table 2, and the contours of samplings are shown in Figure 3 and Figure 4. In Figure 5, we present the fitted luminosity functions at various redshifts for all four types of galaxies as an illustration. **We note that there is a turnover in the fitted luminosity function at lower luminosities. This turnover has not been reported in previous studies, such as those by Kondapally et al. (2023) for AGN LFs, as these studies excluded low-luminosity data from the LoFAR survey due to concerns about completeness. We have retained the low-luminosity part of LoFAR data in our analysis, which accounts for the observed turnover, particularly for the LERG population. A similar effect can be found for the SFG population when comparing our results to those of Cochrane et al. (2023). While this turnover influences our predicted source counts at flux densities below the LoTSS observational limits, we emphasize that caution is necessary when extrapolating to significantly lower flux densities, as these predictions may differ substantially from models based on previously published LFs.**

### 3.2 Total intensity number counts

In the redshift-dependent evolutionary luminosity function model, we take into account the values of  $\Phi(L|z)$  for small luminosity intervals  $\Delta \log(L)$  and redshift intervals  $\Delta z_i$ . This enables us to calculate

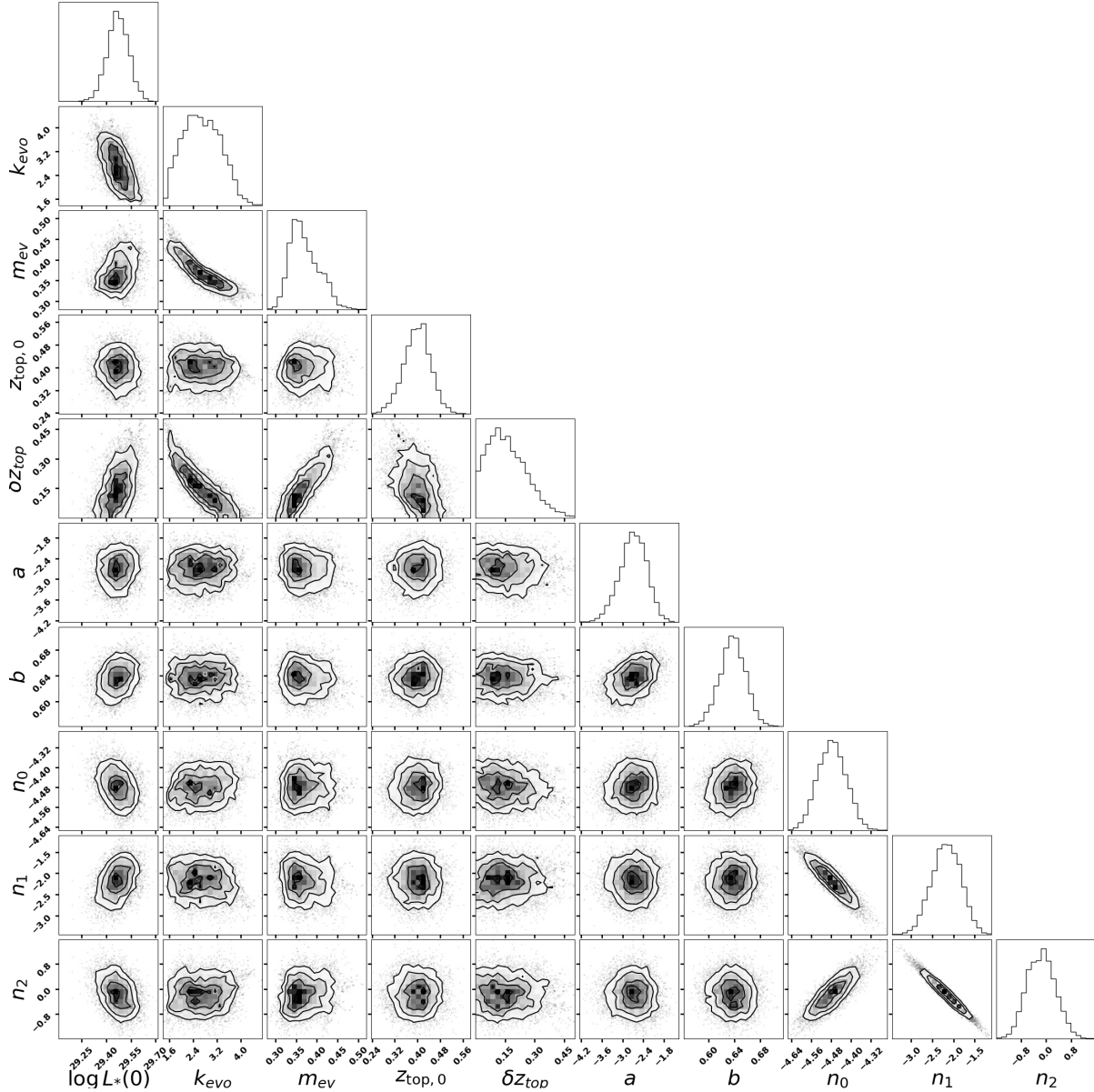


**Figure 1.** Posterior distributions of the luminosity-redshift evolutionary model for High Excitation Radio Galaxy (HERG) sources.

the number of sources of each type within a given interval. The formula for this calculation is as follows,

$$\Delta N(L)_{i,j} = \Omega \Phi(L_j|z_i) V(\Delta z) \Delta \log(L), \quad (10)$$

where  $\Omega$  represents the simulated solid angle,  $z_i$  denotes the central point of the redshift bin, and  $V(\Delta z)$  corresponds to the volume associated with both the solid angle and redshift bin. We assumed that sources are randomly distributed within  $\Delta \log(L)$  and  $\Delta z$ , and we found when  $\Delta z = 0.005$  and  $\Delta \log(L) = 0.005$  for AGNs and SFGs, the fitting results are the best. The total source count is given by:

$$N = \sum_{i,j} \Delta N(L)_{i,j}. \quad (11)$$

### 3.3 Source sizes

To model the sizes of HERG and LERG, we adopt the narrow model outlined by DiPompeo et al. (2013) (see their table 2). This approach utilizes Monte Carlo simulations to generate sources with random angular sizes and orientations. The probability distributions for these simulations are informed by the findings from Barthel (1989), Singal & Laxmi Singh (2013), and Boroson (2011). The orientation angle is modeled as  $N(\theta) = \sin \theta$ , where  $\theta$  represents the orientation angle. The model subsequently integrates a linear fit to accommodate larger intrinsic sizes and a power-law fit for smaller sizes, with the breakpoint of the function precisely determined through a fitting process.

We note that, due to the different classification for SFGs, the latest version of T-RECS (Bonaldi et al. 2023) can not be applied. We therefore adopted the same shape model for SFGs as the old version of T-RECS (Bonaldi et al. 2019). To be specific, this model

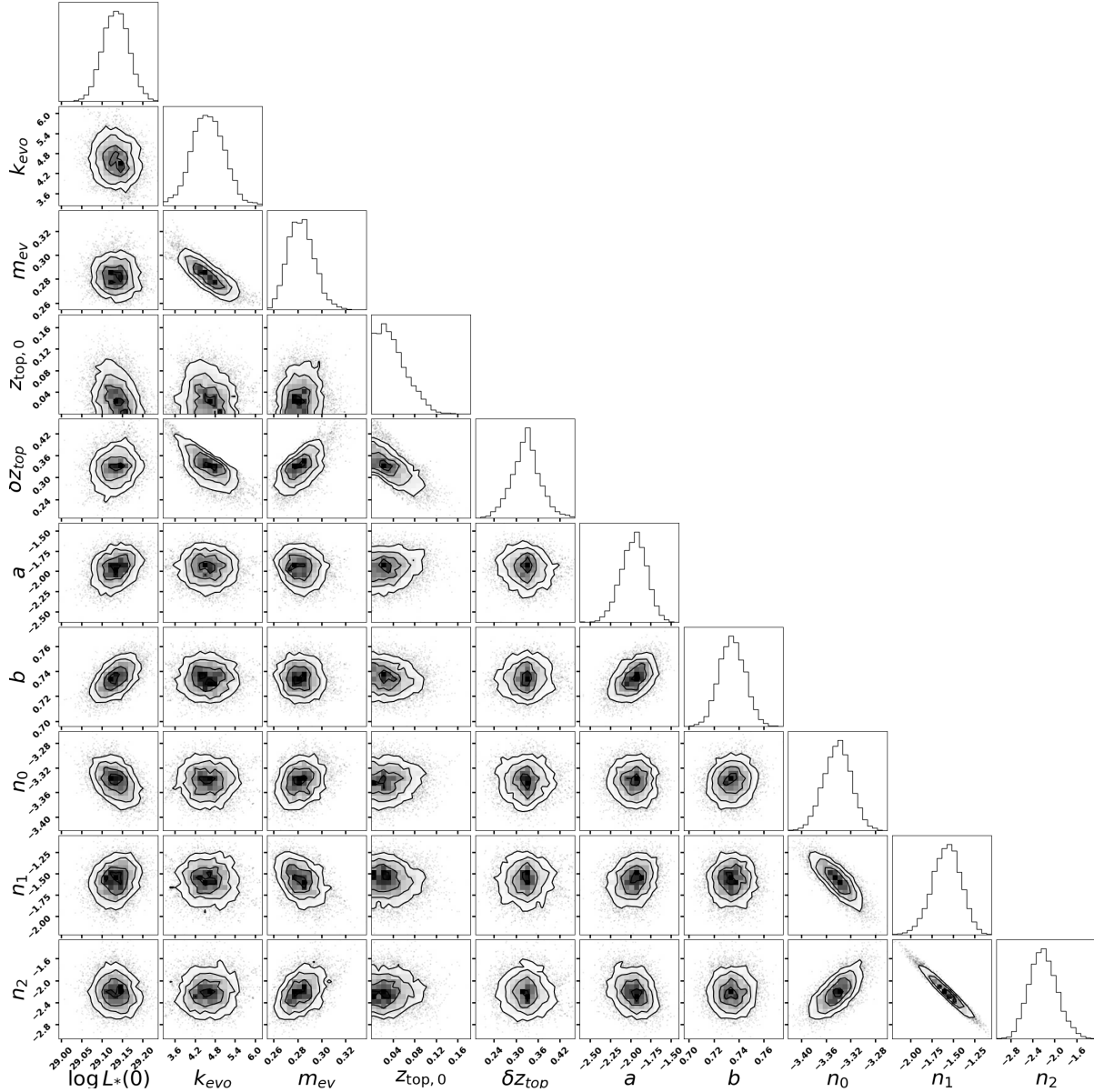


**Figure 2.** Posterior distributions of the luminosity-redshift evolutionary model for Low Excitation Radio Galaxy (LERG) sources.

determines the stellar mass based on the relationship between dark matter halos and stellar mass ( $M_* - M_H$ ), as presented in table 2 of Aversa et al. (2015). Subsequently, it derives the intrinsic size of the source from the relationship between stellar mass and source intrinsic size according to Shen et al. (2003). The related free parameters are determined using results re-fitted by the T-RECS team. Regarding the shape, we employ the ellipticity distribution model from Tunbridge et al. (2016). Ellipticities are randomly assigned to each source according to the distribution model, and the axis ratio is then calculated.

### 3.4 Star formation rate

We updated the star formation rate for all sources using equation 2 in section 6 of Best et al. (2023) and also their source classification method. A statistical relationship between luminosity and star forma-

tion rate has been established for sources in different flux intervals, serving as the standard for assigning SFRs.

**For RQ-AGN and SFGs, the star formation rate is given by**

$$\text{SFR}_{\text{SFG}} = \frac{L - 22.24}{1.08} + \text{Gaussian}(\mu, \nu), \quad (12)$$

where  $L$  represents the radio luminosity of the source, measured in  $\text{W Hz}^{-1}$ . The term  $\text{Gaussian}()$  represents a random number generated from a Gaussian distribution, where  $\mu$  is the mean and  $\nu$  is the variance both obtained by fitting the sources from LoTSS.

For HERGs and LERGs, it is necessary to account for an additional radio excess, typically around 0.7 dex offset from the standard  $L_{\text{rad}}$ -SFR relation described above. The star formation rate for these sources is then given by

$$\text{SFR}_{\text{AGN}} = \frac{L - 22.24 - 0.7 - \text{RandomExponential}(\lambda)}{1.08}, \quad (13)$$

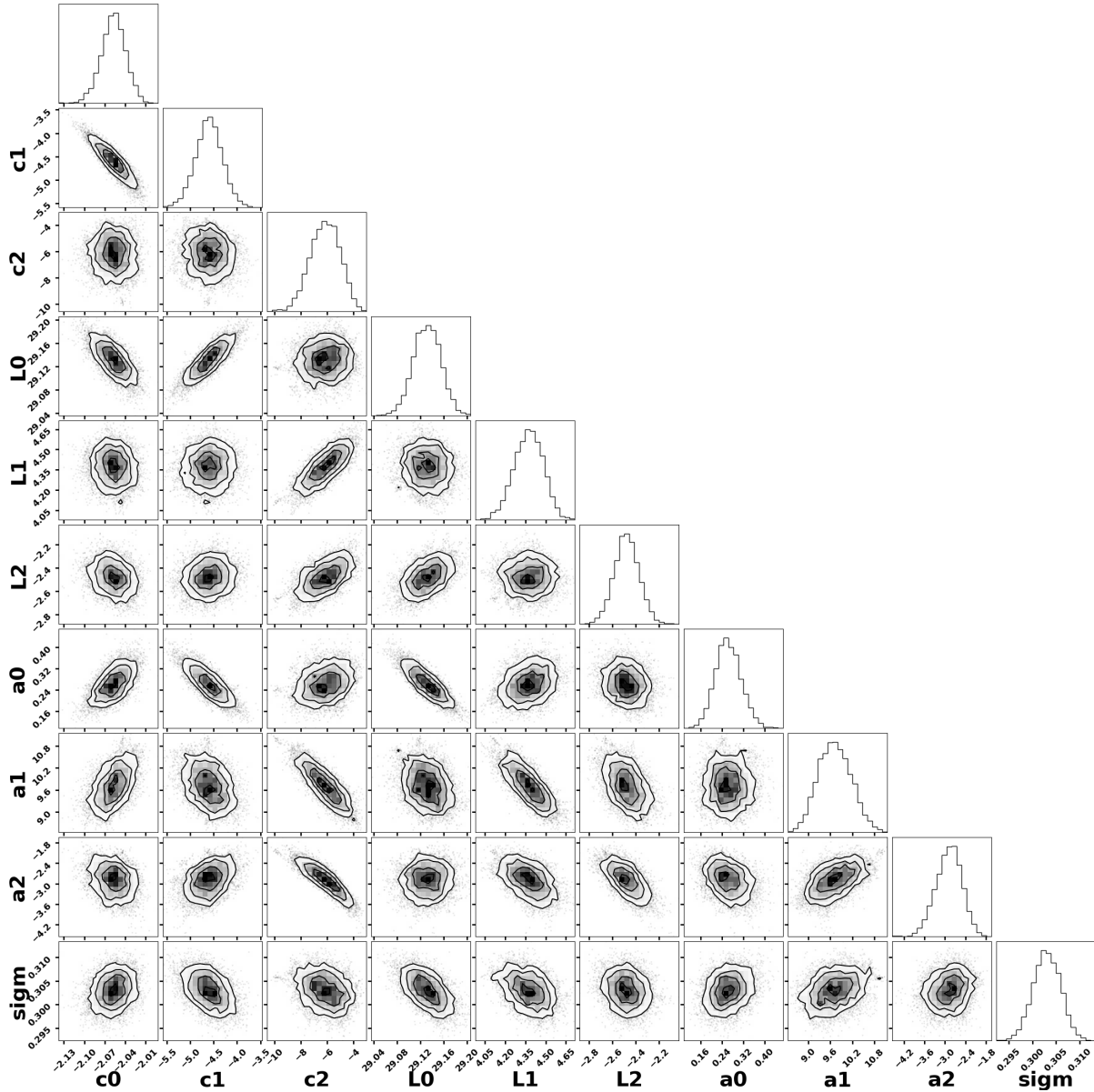


Figure 3. Posterior distributions of the luminosity-redshift evolutionary model for star-forming galaxies (SFGs) sources.

where `RandomExponential()` is a random number generator for the exponential distribution, and  $\lambda = 0.7952$ , which is obtained by fitting the sources from LoTSS. The offset of 0.7 dex arises because both HERGs and LERGs exhibit significant radio excess. Therefore, the overall SFR is lower compared to the relation established for RQ-AGN and SFGs, with an additional random variation accounted for by the exponential distribution. We fit the data from different flux intervals to obtain the parameters shown in Tables 3 and 4.

### 3.5 Spectral index

We performed Gaussian fitting on the spectral index distribution,  $\alpha_L$ , of AGNs using the dataset provided by Franzen et al. (2021b), resulting in a mean value of -0.701 and a variance of 0.0421. This distribution was then used to generate the spectral indices for HERGs

Table 3. These are the relevant parameters for the Gaussian fitting in the SFR model for RQAGN.

flux range(Jy)	mean $\mu$	variance $\nu$
0.0 – 0.000143	0.0594	0.0655
0.000143 – 0.000226	-0.0477	0.0582
0.000226 – 0.000358	-0.179	0.0603
0.000358 – 0.000568	-0.244	0.0659
0.000568 – 0.000900	-0.328	0.0640
0.000900 – 1000.0	-0.353	0.0782

and LERGs. Following a similar method, we analyzed the spectral index distribution of SFGs from the same dataset, achieving a mean of -0.603 and a variance of 0.0372. We subsequently utilized this distribution to generate spectral indices for RQ-AGNs and SFGs.

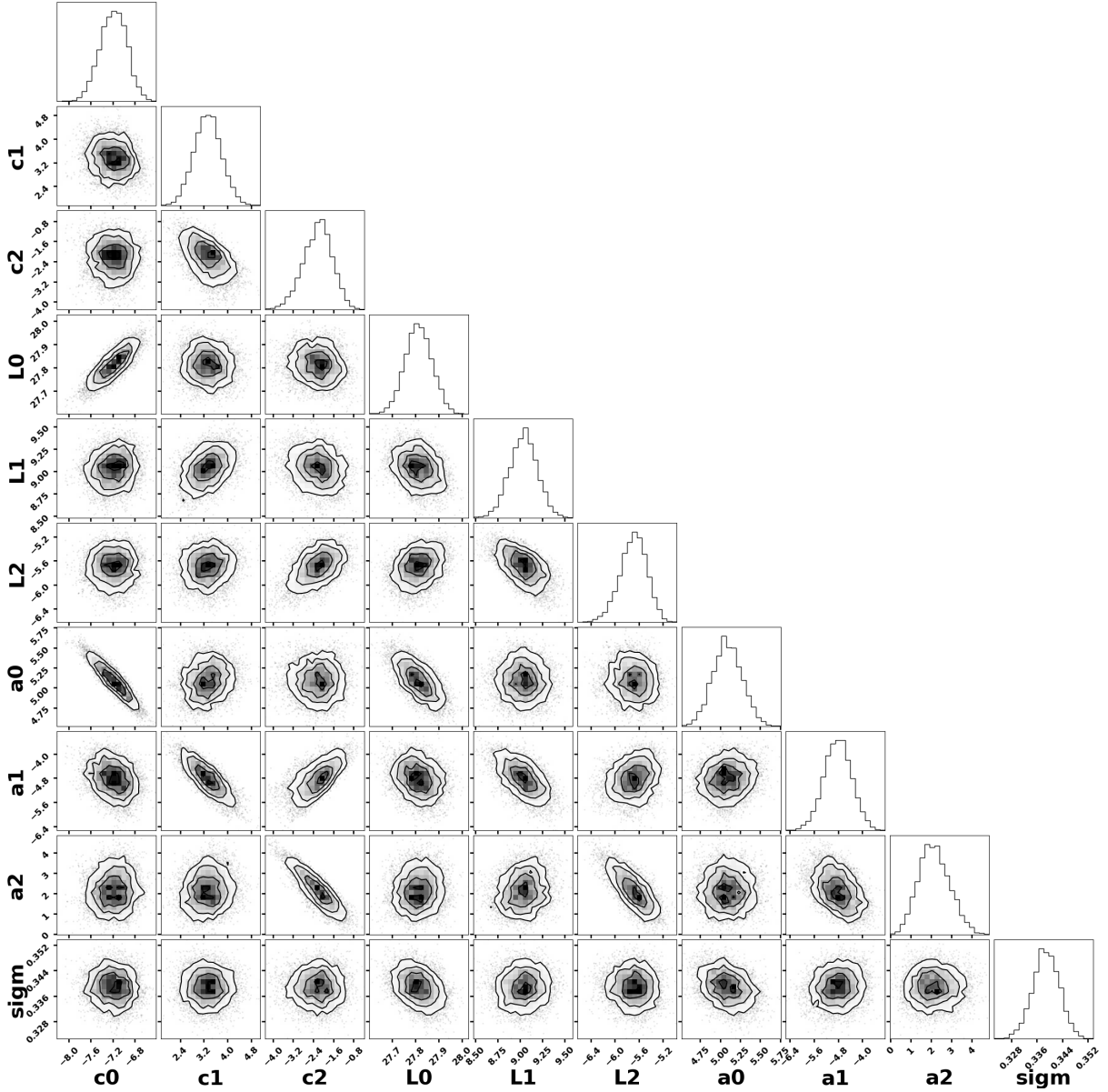


Figure 4. Posterior distributions of the luminosity-redshift evolutionary model for radio-quiet AGN (RQAGN) sources.

Table 4. These are the relevant parameters for the Gaussian fitting in the SFR model for SFG.

flux range(Jy)	mean $\mu$	variance $\nu$
0.0 – 0.000143	0.0302	0.0575
0.000143 – 0.000226	-0.0463	0.0591
0.000226 – 0.000358	-0.118	0.0607
0.000358 – 0.000568	-0.173	0.0624
0.000568 – 0.000900	-0.198	0.0654
0.000900 – 1000.0	-0.185	0.0695

### 3.6 Polarization

Due to the lack of low-frequency polarization observations, we apply the 1.4 GHz polarization model proposed by Hales et al. (2014) to LERGs and HERGs. For the polarization model of SFGs and RQ-AGNs, we use the same model as T-RECS for SFG polarization (Sun & Reich 2012). Our low-frequency polarization results closely match

those of T-RECS, as illustrated in Figure 6, owing to the consistency of the selected model.

## 4 VALIDATION

In this section, we validate our results by comparing them with outcomes from prior simulations, notably SKADS and the latest iterations of T-RECS, as well as the observations from LoTSS-Deep and the study conducted by Franzen et al. (2016) in this section.

For this purpose, we created a simulation with the model described in the previous section, delineated a celestial expanse spanning 25.65 square degrees and established a flux density cutoff at 0.11 mJy. This criterion was selected to align with the parameters of the LoTSS dataset, facilitating straightforward comparison.

For the LoTSS-Deep comparison, we leverage the completeness simulations executed by Kondapally et al. (2022) and Cochrane et al.

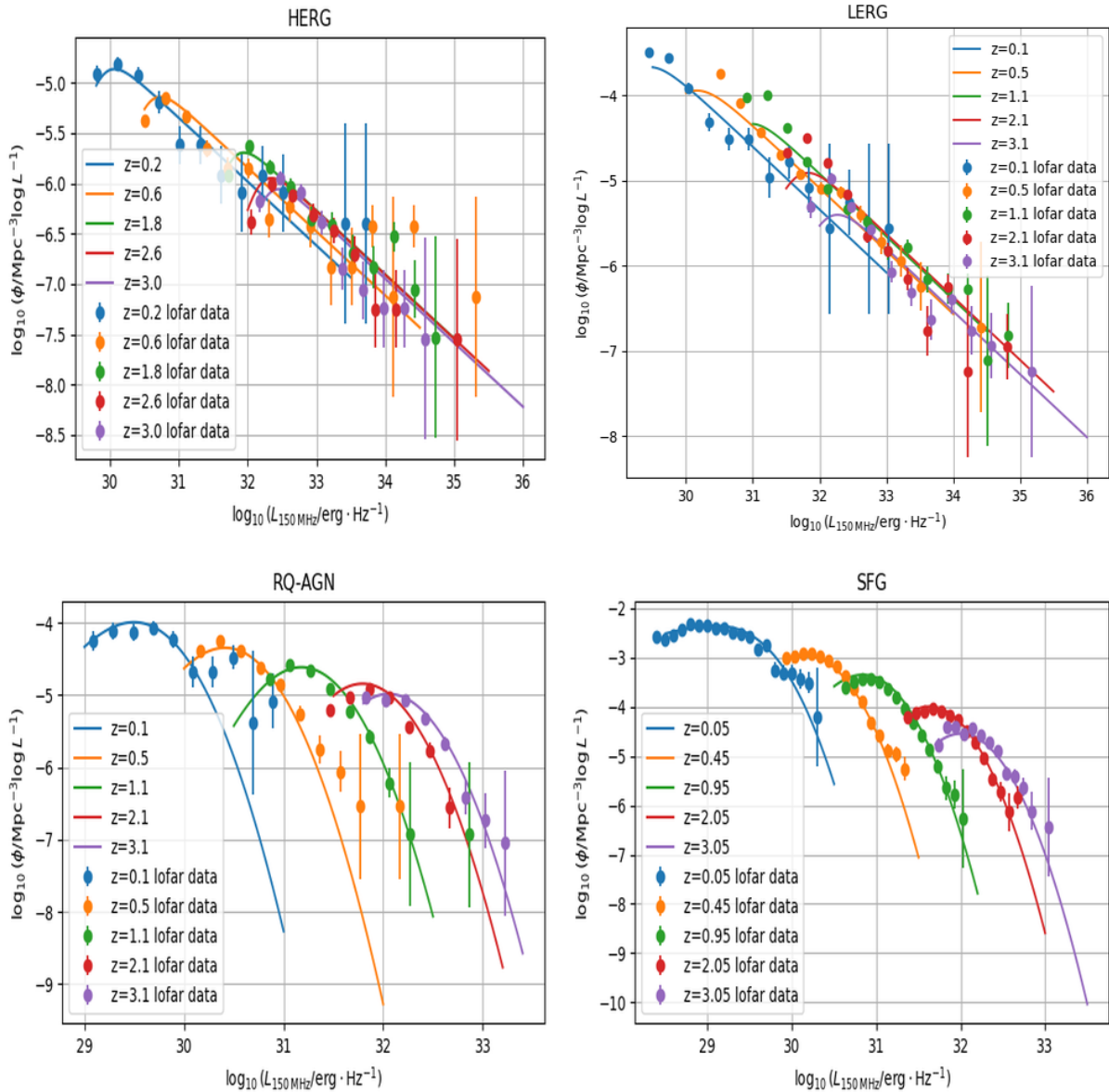


**Figure 5.** The luminosity functions (LFs) for the HERG, LERG, SFG, and RQ-AGN populations at various redshifts.

(2023) for the LoTSS-Deep, to evaluate the detection probability for each simulated source. Following this, we systematically exclude sources from our catalogue as well as the other prior simulations based on these likelihoods, ensuring a rigorous validation when comparing with LoTSS-Deep.

We first focus on the redshift distribution, as shown in Figure 7. For this specific comparison, we employ a flux limit of 0.15 mJy with all types of AGNs and SFGs included. The LoTSS-Deep data, represented by the green line, indicates a notable dip in the redshift range of  $1.0 < z < 1.5$ . This reduction is attributed to an aliasing effect in the photometric redshifts, due to the absence of H-band data, a topic elaborated upon by Best et al. (2023) and further discussed in Cochrane et al. (2023). Consequently, we omitted this segment of data from the fitting analysis presented in the preceding section. The red line illustrates the outcomes after the exclusion of certain sources, in alignment with the completeness simulation studies conducted by Kondapally et al. (2022) and Cochrane et al. (2023). The simulated

celestial projections from SKADS and T-RECS are depicted by the blue and yellow lines, respectively, with both models incorporating considerations of LoTSS-Deep completeness. Notably, the SKADS predictions manifest a significant shortfall in source counts beyond a redshift of  $z > 2$ , a trend that T-RECS also exhibits beyond  $z > 4$ . In contrast, our results demonstrate a closer approximation to the empirical observations of the celestial sphere.

The comparative analysis of differential source counts in total intensity at 150 MHz, encompassing AGN and SFG, is illustrated in Figure 8. The observations from LOFAR are denoted by blue dots, while the results from T-RECS and this study (both post-adjusted for completeness by randomly subtracting sources) are represented by cyan and red dots, respectively. Observations from Franzen et al. (2016) are indicated by green dots. It can be found that in the higher flux density spectrum, both T-RECS and our study align closely with the observational data. However, at the lower flux density threshold, near  $10^{-4}$  Jy, our study demonstrates a more precise alignment



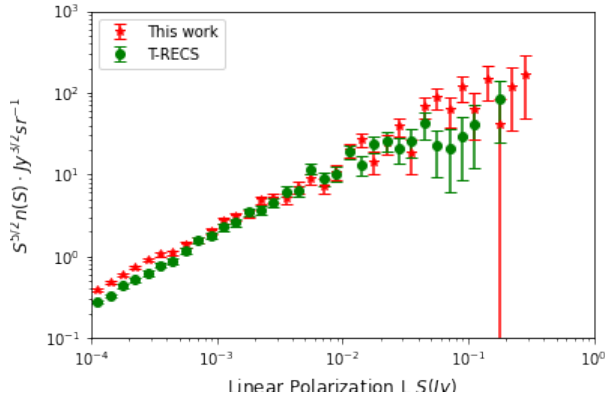


**Figure 6.** The comparison the differential source counts of polarization in this work with those from T-RECS at 150MHz.

with the observational data compared to T-RECS, highlighting the effectiveness of our adjustments. We note that our analysis is focused at 150 MHz only, while the T-RECS model covers the 150 MHz–20 GHz frequency range. While our model represents an improvement with respect to the original T-RECS model at the low-frequency end, consistency with observations at higher frequencies has not been addressed here.

Now we focus on the power spectrum of the image cubes of point sources. To mimic the simulation along the frequency axis, we employ a power-law model with randomly distributed spectral indices, whose distributions are sourced from the sample provided by Franzen et al. (2021b), as we discussed earlier in 3.5. This approach enables us to generate a three-dimensional cube, spanning a frequency range from 150 MHz to 160 MHz, with a frequency resolution of 0.02 MHz. To model the morphology of the point sources, we utilize *galsim* (Rowe et al. 2015), generating images that cover a field of view (FoV) of 100 square degrees for each of the 501 frequency slices. These slices are then merged to form a comprehensive data cube. The spatial distribution of these point sources is designed to reflect clustering effects (Bonaldi et al. 2019; Baugh et al. 2019; Jiang et al. 2014). This methodological approach ensures a realistic representation of point source clustering across the simulated data cube. For comparison, we also calculated the power spectrum for the T-RECS model as well as the SKADS model (Wilman et al. 2008) using the same FoV and frequencies. For our analysis, we excluded all sources exceeding a brightness temperature of 50,000 K to facilitate comparisons, as these extremely bright sources can disproportionately influence the power spectrum.

For the purpose of error estimation, we conducted fifty simulation sets according to our methodology, and an equivalent number following the T-RECS approach. It’s important to note that we do not account for errors in the SKADS simulation due to the availability of only one published dataset. Figure 9 presents the averaged results from fifty sets of one-dimensional power spectra, calculated subsequent to the exclusion of notably bright sources. The variance is denoted through error bars. Red points illustrate the calculations derived from our simulation, while the one-dimensional power spectra obtained from the T-RECS and SKADS models are represented by cyan and green points, respectively. Upon comparison, the power spectrum from T-RECS is observed to be higher than that of our model. This discrepancy could be attributed to the inherent differences between the models, where T-RECS incorporates a larger quantity of faint sources compared to our simulation.

## 5 CONCLUSIONS

In refining our source classification and luminosity function based on LOFAR observations, we have achieved a more accurate alignment with the redshift distribution and total intensity count of the sources compared to actual data. We conducted comparisons between our model, actual observations, and other existing models, focusing on critical metrics such as the redshift distribution of radio sources, differential source counts in total intensity, and power spectra. In terms of differential source counts at total intensities below 1 mJy, our model shows better alignment with observational data than the T-RECS model at 150 MHz. Moreover, while T-RECS presents higher power spectra—likely due to the inclusion of more faint sources—our model’s power spectra are more closely aligned with those from the SKADS model. Our model also demonstrates improved agreement in the distribution of source counts across redshifts, particularly at higher redshifts, compared to observations from LoTSS. Additionally, our model allows for the extension of simulations to larger sky areas with lower flux density thresholds, despite the smaller surveyed area of LoTSS. We note that our focus is on low frequencies, and consequently, we did not verify consistency at higher frequencies as performed by the T-RECS model.

We have made the modified T-RECS code, which incorporates our model for simulating low-frequency radio point sources, available to the research community<sup>1</sup>. This effort significantly enhances the accuracy of simulations and facilitates further studies in the dynamics of the low-frequency radio source sky.

## ACKNOWLEDGEMENTS

We thank ChatGPT for polishing our English in this paper. This work is supported by National SKA Project of China (No. 2020SKA0110100), and the National Natural Science Foundation of China (No. 12203085, 11925301, 11890692, 11873074, 11525312, 11333005, U1831205, U1531130, Y845281001). HYS acknowledges the support from Key Research Program of Frontier Sciences, CAS, Grant No. ZDBS-LY-7013 and Program of Shanghai Academic/Technology Research Leader.

## DATA AVAILABILITY

The data underlying this article will be shared on reasonable request to the corresponding author.

## REFERENCES

- Aversa R., Lapi A., de Zotti G., Shankar F., Danese L., 2015, *ApJ*, **810**, 74  
 Barthel P. D., 1989, *ApJ*, **336**, 606  
 Baugh C. M., et al., 2019, *MNRAS*, **483**, 4922  
 Best P. N., et al., 2023, *MNRAS*, **523**, 1729  
 Blandford R., Meier D., Readhead A., 2019, *ARA&A*, **57**, 467  
 Bonaldi A., Bonato M., Galluzzi V., Harrison I., Massardi M., Kay S., De Zotti G., Brown M. L., 2019, *MNRAS*, **482**, 2  
 Bonaldi A., Hartley P., Ronconi T., De Zotti G., Bonato M., 2023, *MNRAS*, **524**, 993  
 Bonzini M., et al., 2015, *MNRAS*, **453**, 1079  
 Boquien M., Burgarella D., Roehly Y., Buat V., Ciesla L., Corre D., Inoue A. K., Salas H., 2019, *A&A*, **622**, A103

<sup>1</sup> [https://github.com/nxdtxdyka/f150\\_ps\\_simulation](https://github.com/nxdtxdyka/f150_ps_simulation)

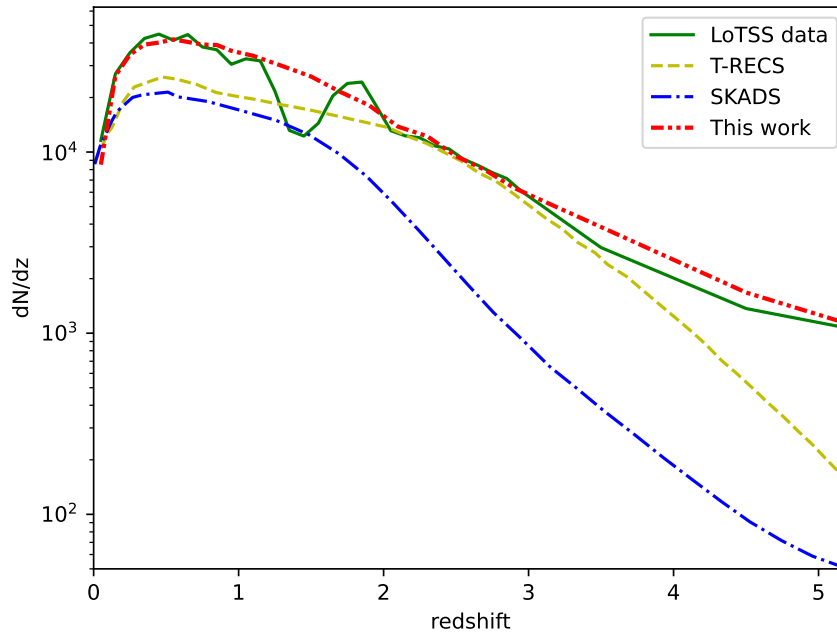


**Figure 7.** Redshift distribution of radio sources. The green line represents the LoTSS-Deep data. The red line denotes the result of our model considering the residual sources after completeness simulations from [Kondapally et al. \(2022\)](#); [Cochrane et al. \(2023\)](#). The blue and yellow lines respectively depict the sky simulation predictions of SKADS and T-RECS.

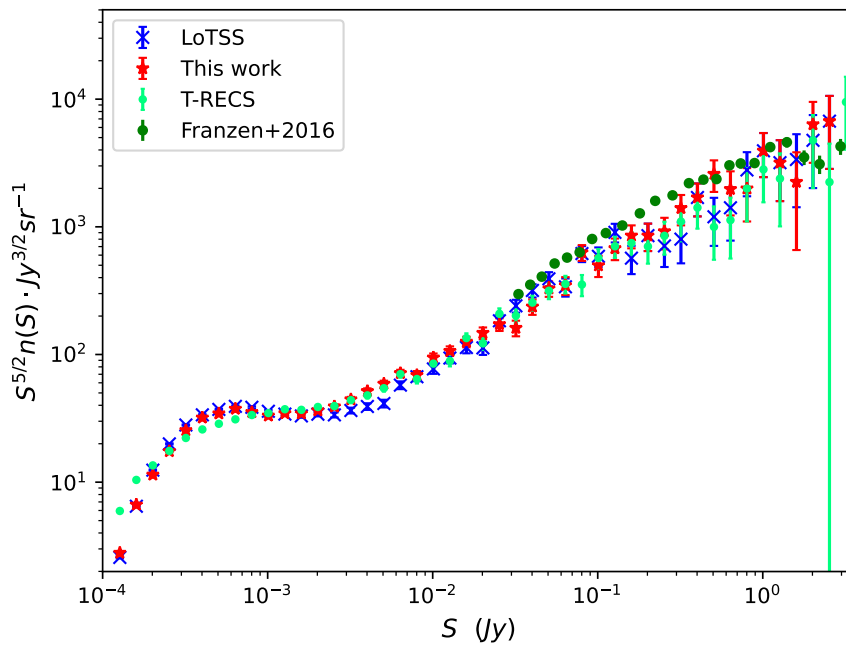


**Figure 8.** The comparison of differential source counts in total intensity at 150 MHz. The blue points represent the observational data from LOFAR. The cyan points and red points are the results from T-RECS and this study, respectively, after considering completeness and randomly removing sources. The green points are from [Franzen et al. \(2016\)](#).

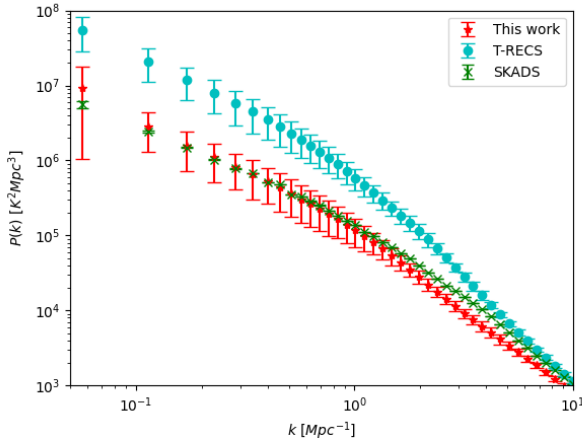


**Figure 9.** The one-dimensional power spectrum for comparison, all accounting for clustering effects. Red dots denote our model. Cyan dots represent calculations conducted with the T-RECS model. Green dots indicate results obtained using the SKADS model.

Boroson T. A., 2011, in American Astronomical Society Meeting Abstracts #217. p. 142.22

Bowman J. D., Morales M. F., Hewitt J. N., 2009, *ApJ*, **695**, 183

Burgarella D., Buat V., Iglesias-Páramo J., 2005, *MNRAS*, **360**, 1413

Calistro Rivera G., Lusso E., Hennawi J. F., Hogg D. W., 2016, *ApJ*, **833**, 98

Carnall A. C., McLure R. J., Dunlop J. S., Davé R., 2018, *MNRAS*, **480**, 4379

Carnall A. C., Leja J., Johnson B. D., McLure R. J., Dunlop J. S., Conroy C., 2019, *ApJ*, **873**, 44

Chapman E., Jelić V., 2019, Foregrounds and their mitigation ([arXiv:1909.12369](https://arxiv.org/abs/1909.12369))

Cochrane R. K., et al., 2023, *MNRAS*, **523**, 6082

Condon J. J., 1992, in Holt S. S., Neff S. G., Urry C. M., eds, American Institute of Physics Conference Series Vol. 254, Testing the AGN paradigm. pp 629–639, [doi:10.1063/1.42217](https://doi.org/10.1063/1.42217)

Condon J. J., Kellermann K. I., Kimball A. E., Ivezić Ž., Perley R. A., 2013, *ApJ*, **768**, 37

Di Matteo T., Perna R., Abel T., Rees M. J., 2002, *ApJ*, **564**, 576

DiPompeo M. A., Runnøe J. C., Myers A. D., Boroson T. A., 2013, *ApJ*, **774**, 24

Duncan K. J., et al., 2021, *A&A*, **648**, A4

Fanaroff B. L., Riley J. M., 1974, *MNRAS*, **167**, 31P

Foreman-Mackey D., Hogg D. W., Lang D., Goodman J., 2013, *PASP*, **125**, 306

Franzen T. M. O., et al., 2016, *MNRAS*, **459**, 3314

Franzen T. M. O., Hurley-Walker N., White S. V., Hancock P. J., Seymour N., Kapińska A. D., Staveley-Smith L., Wayth R. B., 2021a, *Publ. Astron. Soc. Australia*, **38**, e014

Franzen T. M. O., et al., 2021b, *Publ. Astron. Soc. Australia*, **38**, e041

Hales C. A., Norris R. P., Gaensler B. M., Middelberg E., 2014, *MNRAS*, **440**, 3113

Hardcastle M. J., Croston J. H., 2020, *New Astron. Rev.*, **88**, 101539

Heckman T. M., Best P. N., 2014, *ARA&A*, **52**, 589

Helou G., Soifer B. T., Rowan-Robinson M., 1985, *ApJ*, **298**, L7

Ho L. C., Ulvestad J. S., 2001, *ApJS*, **133**, 77

Hurley-Walker N., et al., 2017, *MNRAS*, **464**, 1146

Hurley-Walker N., et al., 2019, *Publ. Astron. Soc. Australia*, **36**, e047

Jarvis M. J., et al., 2010, *MNRAS*, **409**, 92

Jelić V., et al., 2008, *MNRAS*, **389**, 1319

Jelić V., Zaroubi S., Labropoulos P., Bernardi G., de Bruyn A. G., Koopmans L. V. E., 2010, *MNRAS*, **409**, 1647

Jiang L., Helly J. C., Cole S., Frenk C. S., 2014, *MNRAS*, **440**, 2115

Kellermann K. I., Sramek R., Schmidt M., Shaffer D. B., Green R., 1989, *AJ*,

98, 1195

Kellermann K. I., Condon J. J., Kimball A. E., Perley R. A., Ivezić Ž., 2016, *ApJ*, **831**, 168

Kimball A. E., Ivezić Ž., Wiita P. J., Schneider D. P., 2011, *AJ*, **141**, 182

Kondapally R., et al., 2021, *A&A*, **648**, A3

Kondapally R., et al., 2022, *MNRAS*, **513**, 3742

Kondapally R., et al., 2023, *MNRAS*, **523**, 5292

Laor A., Behar E., 2008, *MNRAS*, **390**, 847

Macfarlane C., et al., 2021, *MNRAS*, **506**, 5888

Mancuso C., et al., 2017, *ApJ*, **842**, 95

Massardi M., Bonaldi A., Negrello M., Ricciardi S., Raccanelli A., de Zotti G., 2010, *MNRAS*, **404**, 532

Murray S. G., Trott C. M., Jordan C. H., 2017, *ApJ*, **845**, 7

Noll S., Burgarella D., Giovannoli E., Buat V., Marcillac D., Muñoz-Mateos J. C., 2009, *A&A*, **507**, 1793

Padovani P., 2016, *A&ARv*, **24**, 13

Padovani P., Bonzini M., Kellermann K. I., Miller N., Mainieri V., Tozzi P., 2015, *MNRAS*, **452**, 1263

Panessa F., Baldi R. D., Laor A., Padovani P., Behar E., McHardy I., 2019, *Nature Astronomy*, **3**, 387

Pritchard J. R., Loeb A., 2012, *Reports on Progress in Physics*, **75**, 086901

Procopio P., et al., 2017, *Publ. Astron. Soc. Australia*, **34**, e033

Rowe B. T. P., et al., 2015, *Astronomy and Computing*, **10**, 121

Sabater J., et al., 2021, *A&A*, **648**, A2

Saunders W., Rowan-Robinson M., Lawrence A., Efstathiou G., Kaiser N., Ellis R. S., Frenk C. S., 1990, *MNRAS*, **242**, 318

Shaver P. A., Windhorst R. A., Madau P., de Bruyn A. G., 1999, *A&A*, **345**, 380

Shen S., Mo H. J., White S. D. M., Blanton M. R., Kauffmann G., Voges W., Brinkmann J., Csabai I., 2003, *MNRAS*, **343**, 978

Shimwell T. W., et al., 2017, *A&A*, **598**, A104

Shimwell T. W., et al., 2019, *A&A*, **622**, A1

Sikora M., Lukasz Stawarz Lasota J.-P., 2007, *The Astrophysical Journal*, **658**, 815

Singal A. K., Laxmi Singh R., 2013, *ApJ*, **766**, 37

Sopp H. M., Alexander P., 1991, *MNRAS*, **251**, 14P

Spinelli M., Bernardi G., Santos M. G., 2018, *MNRAS*, **479**, 275

Sun X. H., Reich W., 2012, *A&A*, **543**, A127

Tunbridge B., Harrison I., Brown M. L., 2016, *MNRAS*, **463**, 3339

Wang J.-M., 2008, *ApJ*, **682**, L81

White S. V., Jarvis M. J., Häußler B., Maddox N., 2015, *MNRAS*, **448**, 2665

White S. V., Jarvis M. J., Kalfountzou E., Hardcastle M. J., Verma A., Cao Orjales J. M., Stevens J., 2017, *MNRAS*, **468**, 217

White S. V., et al., 2020, *Publ. Astron. Soc. Australia*, **37**, e018

Wilman R. J., et al., 2008, *MNRAS*, **388**, 1335

Wilman R. J., Jarvis M. J., Mauch T., Rawlings S., Hickey S., 2010, *MNRAS*, **405**, 447

Yoshiura S., Line J. L. B., Kubota K., Hasegawa K., Takahashi K., 2018, *MNRAS*, **479**, 2767

da Cunha E., Charlot S., Elbaz D., 2008, *MNRAS*, **388**, 1595

de Oliveira-Costa A., Tegmark M., Gaensler B. M., Jonas J., Landecker T. L., Reich P., 2008, *MNRAS*, **388**, 247

This paper has been typeset from a  $\text{\TeX}/\text{\LaTeX}$  file prepared by the author.